

Pt Single Atoms on TiO₂ Polymorphs—Minimum Loading with a Maximized Photocatalytic Efficiency

Shanshan Qin, Nikita Denisov, Bidyut Bikash Sarma, Imgon Hwang, Dmitry E. Doronkin, Ondrej Tomanec, Stepan Kment, and Patrik Schmuki*

For more than 20 years, Pt/TiO₂ represents the benchmark photocatalyst/co-catalyst platform for photocatalytic hydrogen (H₂) generation. Here, single atom (SA) Pt is decorated on different polymorphs of TiO₂ (anatase, rutile, and the mixed phase of P25) using a simple immersion anchoring approach. On P25 and anatase, Pt SAs act as highly effective co-catalyst for pure water splitting with a photocatalytic H₂ evolution activity (4600 μmol h⁻¹ g⁻¹)—on both polymorphs, SA deposition yields a significantly more active photocatalyst than those decorated with classic Pt nanoparticles or conventional SA deposition approaches. On rutile, Pt SAs provide hardly any co-catalytic effect. Most remarkable, for P25, the loading of Pt SAs from precursor solution with a very low concentration (<1 ppm Pt) leads already to a maximized co-catalytic effect. This optimized efficiency is obtained at 5.3 × 10⁵ atoms μm⁻² (at macroscopic loading of 0.06 at%)—for a higher concentration of Pt (a higher density of SAs), the co-catalytic efficiency is significantly reduced due to H₂/O₂ recombination. The interactions of the SA Pt with the different polymorphs that lead to this high co-catalytic activity of SA Pt at such low concentrations are further discussed.

1. Introduction

In 1972, Fujishima and Honda introduced hydrogen (H₂) generation approach based on photocatalytic water splitting using titanium dioxide (TiO₂) as a photon absorbing semiconductor.^[1] Key to the underlying photocatalytic reactions is that photogenerated charge carriers, generated in the semiconductor, can migrate to the material's surface and react with red-ox species in the environment. On the one hand, excited electrons from the conduction band can react with H⁺ in the aqueous solution to form H₂, while holes on the valence band are consumed in an adequate oxidation reaction.^[2–4] This simple and green concept has become the most investigated strategy for the development of clean and sustainable energy. Despite a large number of semiconductors

explored for photocatalytic H₂ generation from water,^[5–7] TiO₂ is still the most intensively investigated photocatalyst, not only due to its suitable energetics for a direct (external bias-free) water splitting but even more due to its outstanding resistance to photo-corrosion.^[2–4] Solar-driven H₂ production from plain water by TiO₂-based photocatalysts has been intensively investigated.^[8] However, the efficiency of the reported TiO₂-based photocatalytic water splitting without sacrificial agents for H₂ productivity is still relatively low for application.^[9–11]

In any case, in order to reach a high photocatalytic activity, generally, a semiconducting light absorber needs to be conditioned to provide a high surface area and sufficient reactive sites. For TiO₂-based photocatalysts, typically, different nanoscale morphologies are used, such as nanotubes, nanosheets, and most frequently, nanoparticles (NPs), that are crystallized to anatase and/or rutile phases. The two polymorphs have a bandgap of 3.2 and 3.0 eV, respectively. Although rutile has a narrower bandgap, anatase often shows superior photocatalytic performance compared to rutile, due to higher electron mobility and lower internal charge carrier recombination losses.^[12] A particularly effective phase combination is the commercial photocatalyst Degussa P25, which consists of anatase (≈80%) and rutile (≈20%) phases. The synergetic effect of the phases in view of photocatalytic activities is often ascribed to grain internal phase junctions, which provide enhanced electron–hole separation.^[13] Nevertheless, also other significant differences, namely in the nature of the electronic surface- and interface states between anatase and rutile have been pointed out.^[14–16]

S. Qin, N. Denisov, I. Hwang, P. Schmuki
Department of Materials Science WW4-LKO
Friedrich-Alexander-Universität Erlangen-Nürnberg (FAU)
Martensstrasse 7, 91058 Erlangen, Germany
E-mail: schmuki@ww4.lko.fau.de

B. B. Sarma, D. E. Doronkin
Institute of Catalysis Research and Technology (IKFT)
Karlsruhe Institute of Technology (KIT)
Hermann-von-Helmholtz-Platz 1, 76344 Eggenstein-Leopoldshafen, Germany

B. B. Sarma, D. E. Doronkin
Institute for Chemical Technology and Polymer Chemistry (ITCP)
Karlsruhe Institute of Technology (KIT)
Engesserstraße 20, 76131 Karlsruhe, Germany

O. Tomanec, S. Kment, P. Schmuki
Regional Centre of Advanced Technologies and Materials
Šlechtitelů 27, Olomouc 78371, Czech Republic

P. Schmuki
Department of Chemistry
Faculty of Science
King Abdulaziz University
P.O. Box 80203, Jeddah 21569, Saudi Arabia

 The ORCID identification number(s) for the author(s) of this article can be found under <https://doi.org/10.1002/admi.202200808>.

© 2022 The Authors. Advanced Materials Interfaces published by Wiley-VCH GmbH. This is an open access article under the terms of the Creative Commons Attribution-NonCommercial-NoDerivs License, which permits use and distribution in any medium, provided the original work is properly cited, the use is non-commercial and no modifications or adaptations are made.

DOI: 10.1002/admi.202200808

Independent of the polymorph, when using plain titania for photocatalytic H₂ formation, the electron transfer from TiO₂ surfaces to the aqueous reactant is very sluggish. This issue is usually addressed by placing suitable co-catalysts on the TiO₂ surface that mediate the electron transfer reaction.^[17] Such co-catalysts most frequently are noble metal nanoparticles such as Pt, Au, or Pd.^[18–20] Due to the high work function of these noble metal particles, photoexcited electrons can be scavenged from the conduction band of the TiO₂, which diminishes unfavorable electron–hole recombination reactions. This behavior is often characterized by the formation of a Schottky junction between the semiconductor TiO₂ and the noble metals.^[21] In addition to this electron trapping effect, some metals, particularly Pt, facilitate the combination of 2 H⁰ → H₂ and thus, additionally facilitate H₂ formation. Both factors (Schottky junction and facilitated H₂ recombination) are generally perceived as playing a key role in the enhanced H₂ production from Pt-decorated TiO₂ photocatalysts.

Traditionally, these co-catalysts are Pt nanoparticles that are deposited on semiconductors by either wet impregnation with a Pt precursor combined with a reduction treatment using, for example, wet NaBH₄ reduction or dry H₂ annealing,^[22,23] or alternatively, photoreduction of Pt precursors.^[24] The reduction steps lead to the formation of metallic nanoparticles of various sizes on the surface of the photocatalysts.^[22–25] However, platinum as a noble metal is comparably expensive, therefore, technological efforts have aimed for years at replacing the Pt with more abundant material. More recently, various efforts try to enhance the Pt utilization efficiency (minimize the loading) without sacrificing the photocatalytic reaction rates. One approach is to maximize the surface-to-volume ratio of the Pt co-catalyst by shrinking its cluster size—in the most extreme case to a single atom (SA) level.^[26–28] In fact, over the past few years, the use of highly dispersed platinum single atoms on supporting semiconductor surfaces has attracted widely increasing interest and substantial research efforts.^[26–29]

In the case of TiO₂, pioneering work by Yang et al. showed that Pt SAs can be loaded onto anatase powders using impregnation/annealing techniques.^[26] The authors revealed that single PtO units on anatase can provide a very high co-activity for photocatalytic H₂ generation. Moreover, the authors deduced that clusters of PtO allow reaching turnover frequencies (TOF) of up to 1200 h⁻¹ in presence of a sacrificial agent.^[30] In contrast to these findings, later work reported the highest co-catalytic activity for metallic Pt particles of ≈1 nm in diameter, regardless of the phase of the supporting titania (anatase or mixed phase P25).^[31] A common feature of these works is the use of thermal treatments and/or thermal reduction of Pt-impregnated substrate for preparing SA decorated titania. These treatments allow to fix the precursor species on the substrate and further reduce them to active surface pinned Pt SA sites. In the meantime, a range of different titania/SA-cocatalyst approaches have been explored.^[32,33] In contrast to these approaches, we recently reported that SA trapping can be achieved on defect-engineered TiO₂ layers^[34–36] or defects of TiO₂ nanotubes grown by anodization on Ti metal.^[37–39]

In the present work, we trap Pt as SA on nanoparticulate titania of the most relevant polymorphs (anatase, rutile, or mixed phase P25 nanoparticles) by immersion of the pow-

ders in an H₂PtCl₆ precursor solution over extended times and investigate the photocatalytic H₂ evolution from plain water. The most remarkable result is, however, that the precursor solutions can be of a very low Pt content, which results in an overall Pt loading on P25 of only 0.06 at.% to reach a maximized photocatalytic efficiency (i.e., <1 ppm Pt in the solution is sufficient to harvest Pt SAs on P25 mixed-phase TiO₂ powder to achieve the most effective saturated co-catalytic effect).

2. Results and Discussion

In the first set of experiments, we deposited Pt single atoms on the different polymorphs of the TiO₂ nanoparticles (i.e., anatase, rutile, and P25) by exposure to a 0.005 mM H₂PtCl₆ solution for 24 h (details are given in the Experimental Section). After rinsing and drying, we measured the powders for the photocatalytic H₂ generation activity from a deionized H₂O using a 365 nm LED (600 mW cm⁻²) for illumination and H₂ detection by gas chromatography (GC), as described in the Experimental Section. **Figure 1a** shows a comparison of the photocatalytic H₂ evolution from the different polymorphs after deposition. In **Figure 1b**, the photocatalytic performance of the SA decorated titanias are further compared to TiO₂ decorated with Pt nanoparticles using conventional Pt nanoparticle deposition approaches (Pt NPs-P25).^[22,24,25] We also included results using a classic SA deposition method taken from literature,^[40,41] which used an impregnation/reduction approach for SA deposition. As we will show below, our immersion approach leads to Pt SA deposition on all titania surfaces. From **Figure 1a,b**, the SA deposited P25 (Pt SA-P25) produces an approximately two times higher H₂ amount as compared to Pt SA-anatase; that is 4600 μmol h⁻¹ g⁻¹ versus 2000 μmol h⁻¹ g⁻¹ and ≈20 times higher H₂ production than Pt SA decorated rutile (≈100 μmol h⁻¹ g⁻¹). That is, on rutile, the H₂ production rate is almost as low as for the non-Pt-decorated polymorphs. A similar trend in H₂ evolution performance (P25 > anatase >> rutile) is also observed for the different polymorphs, if instead of SAs they are loaded with Pt NPs.

Determination of the Brunauer–Emmett–Teller (BET) specific surface area for the different powder samples (**Figure 1cA**) shows that the specific surface area of the anatase powder is similar to the P25 and approximately two times higher than for rutile. In other words, the differences in photocatalytic H₂ production cannot be ascribed to the different specific areas of the powders. Atomic absorption spectroscopy (AAS) analysis of the total amount of Pt loaded on the different polymorph samples by immersion (**Figure 1cB**) shows a very similar level of Pt loading on the different polymorphs., that is, the strongly different H₂ evolution for the different polymorphs also cannot be ascribed to a significantly different Pt loading. Moreover, **Figure S1**, Supporting Information, shows a comparison of the mass normalized photocatalytic activity (H₂ production per mg loaded Pt as determined from AAS) for all samples considered in this study. Corresponding TOF is calculated in **Figure S2**, Supporting Information.

Please note that the performance of SA Pt deposited from the 0.005 mM precursor solution outperforms Pt deposited in nanoparticle form on any polymorph, as well as using a literature-based SA deposition approach based on impregnation/reduction applied to the different polymorphs.^[40,41]

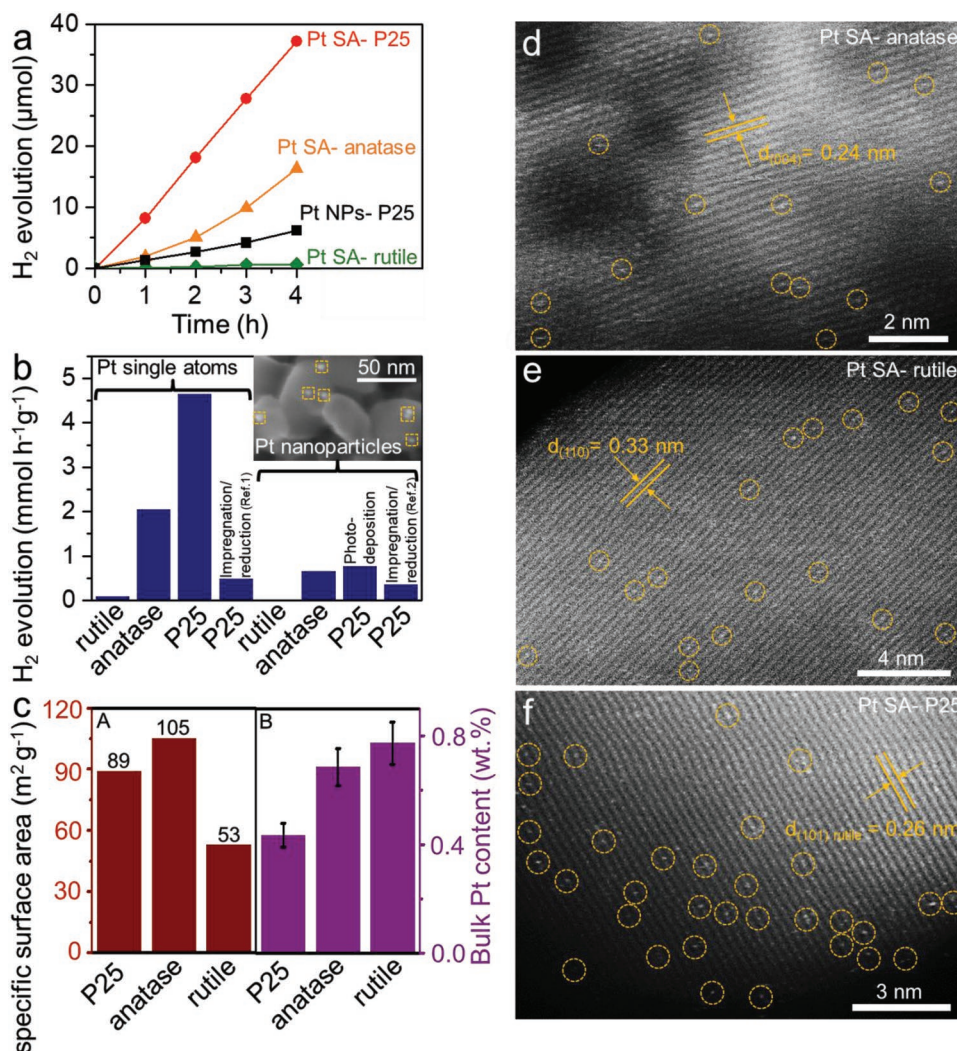


Figure 1. a) H₂ evolution time courses for Pt SA-P25, Pt SA-anatase, and Pt SA-rutile samples prepared by immersion deposition, and for Pt NPs-P25 prepared by photodeposition. b) Comparison of the open circuit H₂ evolution rates for rutile, anatase, and P25 nanoparticles loaded with Pt SA by immersion deposition (0.005 mM), Pt NPs by photodeposition, Pt SA (Ref. 1),^[40,41] and Pt NPs (Ref. 2)^[22] by impregnation/reduction methods. c) A: Comparison of the specific surface area of P25, anatase and rutile measured by BET. B: Comparison of the Pt loading amount on P25, anatase, and rutile loaded with Pt SA by immersion deposition method measured by AAS. d–f) HAADF-STEM images of Pt SA-anatase, Pt SA- rutile, and Pt SA-P25 prepared using 0.005 mM H₂PtCl₆ solution by immersion deposition.

Figure 1d–f shows high-angle annular dark-field scanning transmission electron microscopy (HAADF-STEM) images of the three samples after deposition from the 0.005 mM H₂PtCl₆ solution (additional data is shown in Figure S3, Supporting Information). From all HAADF-STEM images, one can clearly identify Pt SAs that are uniformly distributed over the surface of the samples. From several HAADF-STEM images, we evaluated a SA density of $\approx 6.4 \times 10^5 \mu\text{m}^{-2}$ for anatase, $7.8 \times 10^5 \mu\text{m}^{-2}$ for rutile, and $5.3 \times 10^5 \mu\text{m}^{-2}$ for P25. Transmission electron microscopy energy-dispersive X-ray spectroscopy (TEM-EDX) characterization (performed in the area depicted in Figure S4a–c, Supporting Information) shown in Figure S4d–f, Supporting Information, shows the presence of Pt in the Pt SA-P25, Pt SA-anatase, and Pt SA-rutile samples. Elemental mapping shows a uniform dispersion of Pt on the surface (Figure S5, Supporting Information). Extended SEM

studies (examples are shown in Figure S6, Supporting Information) show no trace of Pt aggregation, which reflects the uniform dispersion of the SAs on the substrate. In contrast, as expected, clearly visible Pt nanoparticles with an average size of ≈ 4 nm are obtained by classic photodeposition, as evident from the inset in Figure 1b (and Figure S7, Supporting Information).

Please note that the total amount of Pt loaded in the form of NPs is similar to the total amount of Pt loaded via SAs (Figure S8, Supporting Information) and shows also the same sequence of H₂ evolution performance P25 > anatase >> rutile as for the SAs. From Figure S1, Supporting Information, Pt decoration in the form of SAs on P25 is approximately six to ten times more effective than using Pt nanoparticles, and loading the SAs on P25 is approximately four times more effective than loading them on anatase.

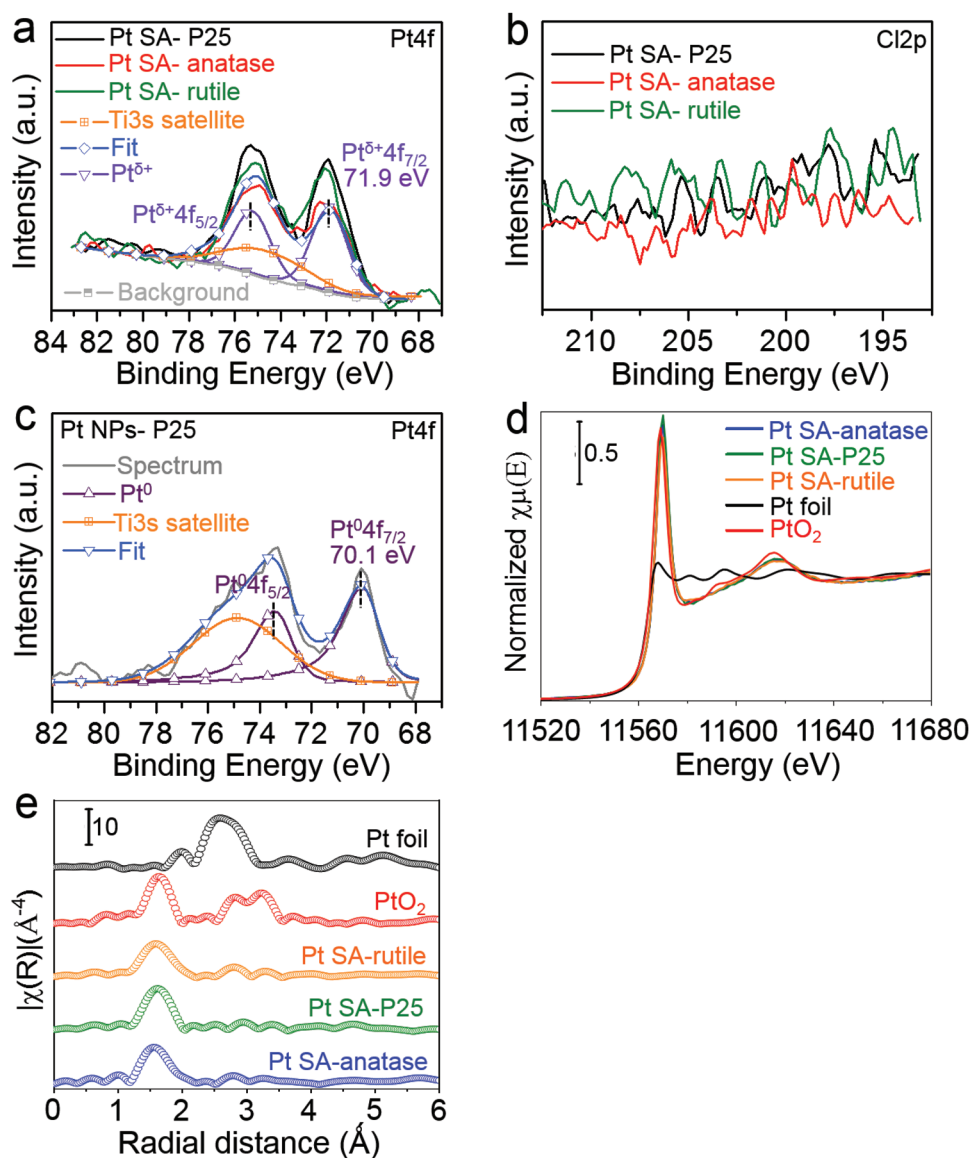


Figure 2. a,b) XPS spectra of Pt SA-P25, Pt SA-anatase, and Pt SA-rutile in the Pt 4f (a) and Cl 2p (b) regions prepared using 0.005 mM H_2PtCl_6 solution by immersion deposition. The fitting in (a) is for photocatalyst of Pt SA-anatase. c) XPS spectra in the Pt 4f region for Pt NPs-P25 (prepared by photodeposition). All the Pt SA-decorated samples were prepared by immersion deposition using a 0.005 mM H_2PtCl_6 solution. d) XANES spectra at Pt L_3 -edge of the as-synthesized photocatalysts (prepared using 0.005 mM H_2PtCl_6 solution). Pt foil and PtO_2 are also shown as references. e) FT k^3 -weighted EXAFS spectra of all the photocatalysts (prepared using 0.005 mM H_2PtCl_6 solution) together with the reference foil and oxide.

X-ray photoelectron spectroscopy (XPS) spectra of the Pt 4f and Cl 2p regions for the SA decorated TiO_2 polymorphs are shown in **Figures 2a** and **2b**, respectively. Clear Pt 4f_{7/2} and 4f_{5/2} doublet peaks at 71.9 and 75.2 eV are observed for Pt on anatase, rutile, and P25, while the Cl 2p region in every case shows only noise—the latter indicates that the Pt signals originate from surface-trapped Pt rather than from surface-adsorbed Pt-chloro-complexes (the split of the chloro-coordinated precursor Pt species when reacting with the surface). The peak position for the attached Pt, that is, Pt 4f peak at ≈ 72 eV corresponds well with literature for $\text{Pt}^{\delta+}$ with $\delta \approx 2$ (as widely described for Pt SAs that are coordinated with surface oxygen atoms from TiO_2).^[34] In contrast to the samples that carry Pt SAs, the samples

decorated with Pt NPs (**Figure 2c**) show Pt 4f peaks at 70.1 and 73.5 eV, which correspond well to the Pt 4f position of metallic Pt^0 (bulk).

In addition, we performed X-ray absorption near-edge spectra (XANES) and X-ray absorption fine structure (EXAFS) measurements of all three powders after immersion deposition. The normalized XANES spectra measured at Pt L_3 -edge (11.564 eV) suggests that all the samples bear positively charged Pt centers as shown in **Figure 2d**. The extended EXAFS analysis and the corresponding Fourier transformed radial distribution function (FT) showed the presence of a Pt-O as the first shell around 1.5 Å (phase uncorrected) and the second shell between 2.8–2.9 Å as shown in **Figure 2e**. The equivalent spectra in

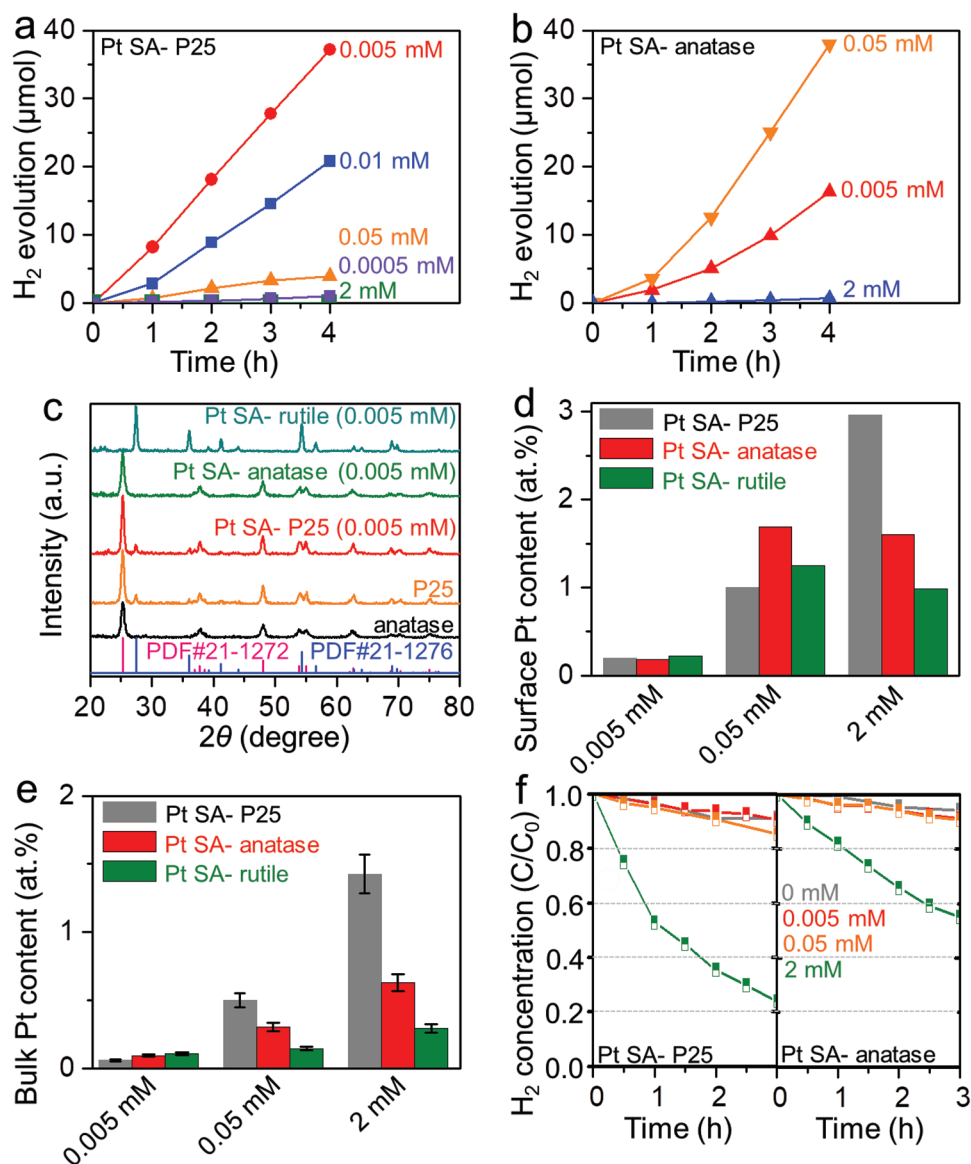


Figure 3. a,b) H₂ evolution time courses by Pt SA loaded TiO₂ samples in DI H₂O under the illumination of a 365 nm LED (600 mW cm⁻²): a) Pt SA-P25; b) Pt SA-anatase. c) XRD patterns of the pristine and Pt SA decorated TiO₂ polymorphs. d,e) Comparison of the Pt loading amount on Pt SA-P25, Pt SA-anatase, and Pt SA-rutile measured by d) XPS and e) AAS. f) Recombination measurements for photocatalysts of Pt SA-P25 and Pt SA-anatase immersion deposited in different concentrations of H₂PtCl₆ solution.

the k-space are shown in Figure S9, Supporting Information, which also indicates the presence of Pt-O as the major contribution. On further analysis of the first shell with EXAFS fitting parameters (taking crystallographic information file of PtO₂), coordination number between 2 and 3 was obtained in all the samples as reported in Table S1, Supporting Information. A comparative analysis of the second shell by taking Pt-O-Pt and Pt-O-Ti paths found that Pt-O-Ti fits better than Pt-O-Pt, as shown in Figures S10 and S11, Supporting Information. The corresponding free parameter values are reported in Tables S1 and S2, Supporting Information. Hence, the second shell scattering is most likely from the Ti of the support.

Overall, the results in Figure 2 reflect the presence of titania-oxygen co-ordinated δ⁺ Pt SA states on the TiO₂ polymorphs

after immersion deposition, while metallic (Pt⁰) nanoparticles are produced by photodeposition. In previous work, we showed that Pt(Cl)₆²⁻ reacts with intrinsic Ti³⁺-O_v states in TiO₂, that is, the attachment of SAs is based on a galvanic displacement.^[36,38]

To evaluate the effect of the Pt SA loading concentration and the H₂ evolution performance of TiO₂ polymorphs, we performed immersion deposition using different concentrations of the precursor solution (i.e., from 0.0005 to 2 mM) and measured the H₂ evolution for the resulting photocatalysts (Figure 3a,b). Evidently, a higher Pt concentration in the precursor solution, results in a higher loading (Figure 3e), and the performance of the H₂ generation from anatase (Figure 3b) can reach the values of P25 (Figure 3a), as seen for example for an H₂PtCl₆ concentration of 0.05 mM. Nevertheless, it

is remarkable that for P25, a maximum H₂ evolution performance can be achieved already from a ten times more dilute precursor solution (0.005 mM). Please note that deposition from the 10 x more concentrated 0.05 mM solution does not further improve the activity of the P25 sample and with even higher Pt concentrations in the precursor, the H₂ production activity drops drastically. The hydrogen production rate slightly accelerates over time (Figure 3a,b), which can be attributed to a process of light-induced Ti³⁺-O_v defect formation in the initial state of illumination.^[42,43]

X-ray diffraction (XRD) patterns for the different TiO₂ polymorphs before and after Pt SA immersion deposition from a 0.005 mM precursor solution are shown in Figure 3c. According to the XRD patterns, all samples are highly crystalline and contain either pure anatase (PDF#21–1272), pure rutile (PDF#21–1276), or a mixture of both anatase and rutile phases (in the case of the P25).

Pt cannot be detected on any sample by XRD but can be evaluated by XPS and the bulk concentration by AAS. Figure 3d,e shows the amount of Pt determined by XPS (Figure 3d) and by AAS (Figure 3e). Noteworthy is that at a higher Pt level in the precursor, P25 accumulates a higher amount of Pt than anatase or rutile—this is most pronounced for the highest investigated concentration (2 mM).

Overall, for the three polymorphs after immersion deposition at low concentrations of the precursor aqueous solution (0.005 mM), a very similar Pt content was found from XPS and AAS. The Pt is present as Pt^{δ+} with δ ≈ 2 on anatase, rutile, and P25. It can be concluded that on all polymorphs, Pt SAs are present, and this with a similar loading. Therefore, the superior H₂ evolution performance shown by Pt SA-P25 (Figure 1a,b) stems neither from a different morphology or chemical state of the Pt co-catalyst nor a different SA loading but from the intrinsically higher activity of the SA Pt on the mixed-phase. Second, it is remarkable that at higher Pt concentrations, a significant drop in activity is observed. In order to assess possible reasons, we considered the influence of the competing recombination reaction of the reaction products, that is, the back reaction H₂ + O₂ → H₂O. As widely described in the literature, this back-reaction is also catalyzed by Pt.^[44–46] Figure 3f shows the results according to recombination measurements for the Pt SA decorated powders. Clearly, at low Pt concentrations, the SAs decorated on anatase and P25 do hardly affect the recombination reaction. The kinetics is similar to the neat titania powder. However, for samples obtained from a higher concentration (2 mM) precursor solution, significant recombination is obtained for both Pt SA on anatase and Pt SA on rutile. This enhanced recombination for higher concentrations can be ascribed to the higher probability of agglomerated SAs that are expected (like Pt nanoparticles) to facilitate the recombination reaction.^[44–46] No oxygen evolution during the photocatalytic tests was detected by GC measurements. The lack of O₂ evolution has been widely observed for TiO₂-based photocatalysts. It is commonly ascribed to the formation of surface-bound Ti-peroxy-species^[47,48] or H₂O₂^[49] as a predominant reaction pathway for photogenerated holes. To exclude the effects of the light absorption properties, we measured the influence of the Pt loading (see Figure S12, Supporting Information). Although P25 loaded with higher amounts of Pt SAs shows a higher

absorbance, the increase in absorption of the relevant excitation wavelength of 365 nm cannot account for the observed strong alterations of Pt loading on the H₂ generation.

The three powders, as characterized by XRD in Figure 3c, were further investigated by photoluminescence (PL) spectra, in order to gain some insights into relevant recombination pathways. The PL in Figure 4a for anatase shows a double peak at 530 and 650 nm, this peak-pair is surface state related^[16] and is strongly quenched upon attachment of Pt SAs. In other words, the extraction of e⁻ onto Pt SAs suppresses the red PL surface state recombination path effectively. In the case of rutile, the near-infrared photoluminescence (NIR-PL) with a peak at 830 nm (Figure 4b) is caused by bulk recombination^[14] and Pt SAs (correspondingly) do not suppress this PL. These findings are in agreement with literature that describes for anatase a dominant e⁻-h⁺ recombination path via surface states. This recombination path can evidently effectively be suppressed by SAs. As this path is dominant for rutile, the photocatalytic activity can hardly be affected by surface-attached Pt SAs for this polymorph.

In the case of the mixed-phase P25 (Figure 4c), clearly, a strong effect of the surface decoration with Pt SAs can be observed. The literature considers that in P25, the internal recombination in the rutile part is strongly reduced due to a swift charge carrier separation across the internal anatase-rutile junction.^[16] As a result, the surface state-related PL (peaking at 542 nm in Figure 4c) on the anatase part of the grain becomes apparent. This surface-related recombination path on P25 then can be quenched by small amounts of Pt SA surface decoration., that is, Pt SA decorated on the TiO₂ (anatase and P25) reduce the recombination of electron-hole pairs and serve as mediators to accelerate the photogenerated electron transfer to H⁺ in aqueous solutions.^[33]

In order to further characterize the nature of the Pt SAs on the three polymorphs, we studied CO adsorption using diffuse reflectance infra-red spectroscopy (DRIFTS, Figure 4d–f), which was carried out with 1% CO diluted in Ar in a continuous flow. All the samples showed CO vibrational frequency at 2096 cm⁻¹, which is characteristic of linearly bonded CO over Pt single site (usually Pt^{δ+}).^[50–52] On the continuous flow of CO, a second peak appears in the range of 2050–2070 cm⁻¹, which can be assigned to linearly bonded CO over small Pt⁰ clusters.^[52,53] These clusters are formed under the CO atmosphere. On flowing Ar afterward, the CO peaks remain in a similar region as shown in Figure S13, Supporting Information, indicating that CO binds strongly to the Pt species. Clearly, for all three titania forms, the Pt SA decoration shows the presence of Pt SAs (evident from the peak at 2096 cm⁻¹).

This additionally confirms the presence of a similar type of SAs on the three polymorphs. Vice versa, this further shows that a difference in the chemical valence of the SAs is not responsible for the differences in the activity of the SAs on the different polymorphs.

Finally, we evaluated the long-term performance of the Pt SA-P25 photocatalyst (generated with a minimum amount of Pt loading on P25) in order to establish if this exceptional performance is stable over time. For this, we performed a 12 h illumination test with the P25 sample decorated using the 0.005 mM Pt precursor solution (Figure 5a). Overall, an almost linear trend

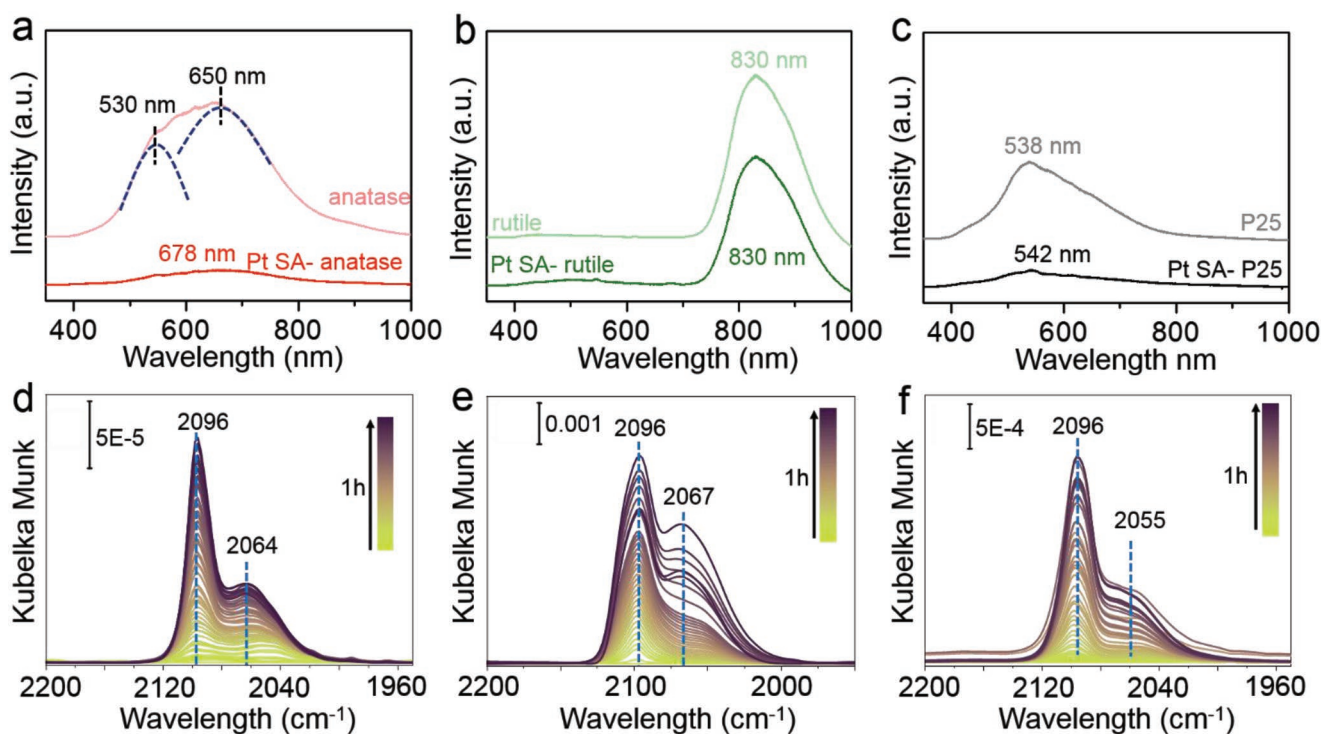


Figure 4. a–c) Photoluminescence spectra of pure TiO₂ and Pt SA decorated TiO₂ powders for a) Pt SA-anatase, b) Pt SA-rutile, and c) Pt SA-P25 prepared using 0.005 mM H₂PtCl₆ solution by immersion deposition. d–f) DRIFTS spectra of d) Pt SA-anatase, e) Pt SA-rutile, and f) Pt SA-P25 prepared using 0.005 mM H₂PtCl₆ solution by immersion deposition.

of H₂ evolution is observed in the initial 6 h of irradiation, followed by a slight drop in activity (Figure 5b). Moreover, XRD characterization for the Pt SAs decorated TiO₂ polymorphs after 12 h illumination (Figure S14, Supporting Information) did not show any structural deterioration of the photocatalysts.

3. Conclusion

We describe in the present work a successful decoration of Pt single atoms on pure anatase, pure rutile, and mixed-phase (P25) TiO₂ polymorphs by a simple immersion technique (this is, without any post-annealing or other subsequent treatments of the samples). This immersion approach leads to

oxygen-coordinated Pt SAs (with $\delta^{\pm} \approx 2$) and an outstanding activity of the single atom Pt decorated P25 and anatase polymorphs reaching 4600 $\mu\text{mol g}^{-1} \text{h}^{-1}$ for Pt SA density of $\approx 5.3 \times 10^5 \mu\text{m}^{-2}$ on P25. This is a remarkable activity of the photocatalyst in the context of literature data,^[33,54] and even more so, considering that the total loading of Pt on this sample is only 0.06 at.%. If compared to the conventional nanoparticulate Pt co-catalysts, Pt SA loading yields a higher H₂ evolution performance and significantly higher Pt utilization. In view of SA deposition techniques, the immersion process also allows to control the amount of Pt loaded onto the supporting TiO₂ by adjusting the concentration of the platinum precursor solution. This allows to maximize the use of Pt—in our investigations, the highest (maximum) activity of SA-decorated titania

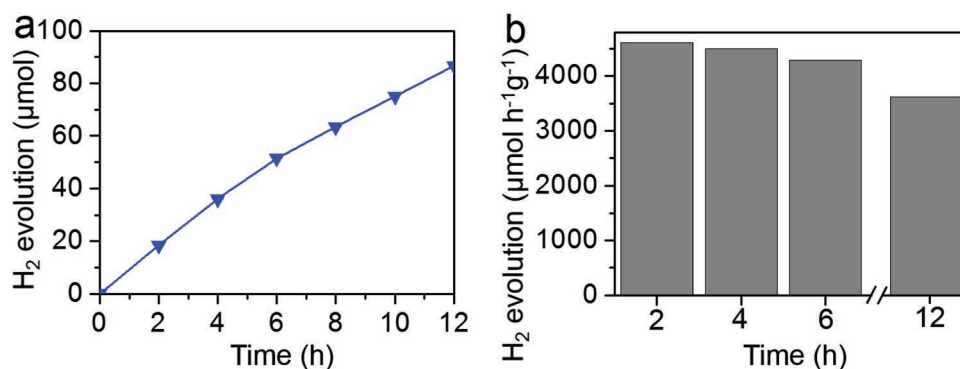


Figure 5. a) H₂ evolution time course for Pt SA-P25 in DI H₂O under the illumination of a 365 nm LED (600 mW cm⁻²) and b) the corresponding H₂ evolution rates.

was achieved using as low concentration as 0.005 mM H₂PtCl₆ on the mixed P25 phase and 0.05 mM H₂PtCl₆ for anatase of loading of 0.06 at.% and 0.31 at.%, respectively.

Based on the above observations, one may therefore deduce that i) a minute amount of Pt SAs is able to provide a very high degree of co-catalytic efficiency on P25 (a SA density of $5.3 \times 10^5 \mu\text{m}^{-2}$ can provide an H₂ production rate of $4600 \mu\text{mol g}^{-1} \text{h}^{-1}$); ii) for higher Pt SA concentrations, the recombination reaction of H₂ + O₂ → H₂O affects the H₂ production detrimentally; iii) the beneficial effect of P25 is due to its embedded junction. This effect particularly is relevant (in comparison to anatase), if the Pt SA surface density is low.

Pt SA loading on rutile has hardly any effect on the H₂ production rate. The results overall show that not the presence of SAs is the main factor to enhance the photocatalytic H₂ production on the different titania polymorphs but its most efficient effect is the suppression of charge carrier recombination if relevant surface states are present. The observed effect of only loading of 0.06 at.% on P25 is remarkably high also in the context of previous approaches reported in the literature (Table S3, Supporting Information).

4. Experimental Section

Preparation of SA Pt Decorated Photocatalysts: Pt SA decoration of TiO₂ nanoparticles (anatase, rutile, and P25) was carried out in an immersion process. For this, commercial TiO₂ nanoparticles of three types (Degussa TiO₂ P25, pure anatase, or pure rutile, Sigma-Aldrich) were used. The nanoparticles were dispersed in an aqueous solution of H₂PtCl₆, which was used as a platinum precursor. The concentration of H₂PtCl₆ in the solution was varied (0.0005, 0.005, 0.01, 0.05, and 2 mM) for the controlled loading of Pt SAs. The prepared suspension (0.2 g L⁻¹) was placed in a sealed vessel, purged with Ar for 20 min, and then continuously stirred in the dark for 24 h. Upon completion, the nanoparticles were washed by centrifuging and rinsing with deionized water three times. Finally, the washed powders were collected and dried in air at 70 °C for 12 h, and thus, Pt SA decorated samples (denoted as “Pt SA-P25”, “Pt SA-anatase”, or “Pt SA-rutile”, correspondingly) were obtained.

For comparison, TiO₂ nanoparticles were also decorated with metallic Pt nanoparticles using a conventional photodeposition process. In this approach, the titania nanoparticles (20 mg) were suspended in 10 mL of methanol:water (1:1 volume ratio) mixture containing 0.5 μM H₂PtCl₆ (which corresponds to ≈0.5 wt% Pt loading on the suspended nanoparticles). The suspension was then purged with Ar and illuminated by a 365 nm LED (170 mW cm⁻²) for 3 h. After illumination, the nanoparticles were washed via centrifuging and rinsing with deionized water three times, followed by drying in air at 70 °C for 12 h. These samples are referred to as “Pt NPs”.

For additional comparison, the deposition of Pt SAs or NPs on titania was also carried out via conventional impregnation/reduction methods.^[22,40,41] For the Pt NPs deposition, NaBH₄ was used as a reducing agent. For this, a suspension of titania nanoparticles (500 mg P25) in a 30 μM H₂PtCl₆ (which corresponds to ≈0.5 wt% Pt loading on the suspended nanoparticles) aqueous solution (400 mL) was prepared and stirred for 2 h. Next, ammonia solution (32 vol%) was added to the suspension under continuous stirring until a pH of ≈11 was established. Next, 10 mL of a 7.2 mM NaBH₄ aqueous solution was added to the suspension (which corresponds to a ratio of B:Pt = 6:1), and the suspension was stirred for another 2 h. The nanoparticles were further centrifuged and rinsed with deionized water three times, followed by drying in air at 70 °C for 12 h.^[22] For the Pt SA deposition, P25 powder (200 mg) was dispersed in an aqueous solution of HCl (0.1 M, 20 mL). An aqueous solution of H₂PtCl₆ (10 mg mL⁻¹, 0.2 mL) was subsequently added into the dispersion and stirred for 24 h at room temperature. The precipitate was separated, washed, and dried under vacuum at 60 °C for

12 h. The as-above precipitate was calcined in a furnace at 400 °C for 1 h and then was treated in a tube furnace at 160 °C for 1 h under the 5% H₂/Ar atmosphere.^[40,41]

Photocatalytic H₂ Evolution: Photocatalytic H₂ evolution by the Pt decorated TiO₂ samples obtained above was studied using their aqueous suspensions (2 mg of powder per 10 mL of H₂O). The suspensions were poured into a sealed quartz cell, purged with Ar, and illuminated with a 365 nm LED (600 mW cm⁻²) under continuous stirring. GC (GCMS-QO2010SE, Shimadzu) measurements were conducted at specific irradiation intervals to evaluate the amount of H₂ generated.

H₂/O₂ Recombination Measurements: H₂/O₂ recombination by the Pt-decorated TiO₂ samples was studied using their aqueous suspensions (2 mg of powder per 10 mL of H₂O). The suspensions were poured into a sealed quartz cell and purged with Ar for 20 min. 1 mL of pure hydrogen and oxygen was injected into the quartz cell. Under continuous stirring for different times in the dark, GC measurements were conducted at specific intervals to evaluate the amount of H₂ and O₂ that remained unreacted.

Photocatalyst Characterization: The morphology and elemental composition of the powdered photocatalysts were assessed by a field-emission scanning electron microscope (SEM, Hitachi S-4800) equipped with an energy dispersive X-ray spectroscopy (EDAX Genesis) (XRD). The crystal structure of the samples was evaluated using XRD measured on an X'pert Philips MPD (equipped with a Panalytical X'celerator detector) using a graphite monochromatic CuKα radiation (λ = 1.54056 Å). The distribution of Pt SAs on the surface and the elemental composition of the samples were further studied by high-angle annular dark-field scanning transmission electron microscopy (HAADF-STEM) and transmission electron microscopy energy-dispersive X-ray spectroscopy (TEM-EDX), respectively, using a high-resolution transmission electron microscope (HRTEM, FEI TITAN G2 60–300). Surface chemical composition and oxidation states were evaluated by X-ray photoelectron spectroscopy (XPS) (PHI 5600), and all XPS spectra were calibrated with the Ti 2p peak to 458.5 eV. Peak deconvolution was carried out by MultiPak software. The total loading of the powders with Pt was determined by electrothermal atomization AAS using a graphite furnace with a contra 600 spectrometer (Analytik Jena AG) equipped with a high-resolution Echelle double monochromator and a continuum radiation source (Xe lamp). The specific surface area was determined using the Brunauer–Emmett–Teller approach at p/p₀ = 0.05–0.2. Room temperature steady photoluminescence spectra measurements in the ambient atmosphere were performed using a HeCd laser (λ = 325 nm) as the excitation source. Diffusive reflectance spectra of Pt decorated P25 powders were measured by a fiber-based UV–vis–IR spectrophotometer (Avantes, ULS2048) equipped with an integrating sphere AvaSphere-30 using AvaLight-DH-S-BAL balanced power light source.

X-ray Absorption Spectroscopy (XAS): XAS of the catalyst powders were measured at Pt L₃-edge (11.564 eV) at the BM23 beamline at the European Synchrotron Research Facility (ESRF), Grenoble, France. The energy was calibrated with a reference metal foil. An Si (111) double crystal monochromator was used to scan the incident energy. The measurements were conducted in transmission mode (for reference samples diluted with cellulose) and in fluorescence mode (in a quartz capillary without any dilution). XAS data reduction and fitting were carried out using the Demeter software packages.^[55] Data reduction (alignment and normalization) was performed using the Athena code (version 0.9.26). The *k* range between 3 and 11.0 Å⁻¹ and *R*-value between 1–3.2 Å were considered for the fit. Amplitude reduction factor, *S*₀², was derived from the corresponding metallic foil to determine the coordination number. The EXAFS equation that was considered for deriving the data is given by

$$\chi(k) = S_0^2 \sum_i N_i \frac{f_i(k)}{kD_i^2} e^{-\frac{2D_i}{\lambda(k)}} e^{-2k^2\sigma_i^2} \sin(2kD_i + \delta_i(k)) \quad (1)$$

where, *S*₀² is the amplitude reduction factor, *N* is the degeneracy of the scattering path, *f*(*k*) is the scattering function, *k* is the wavenumber, *D* or *R* is the distance between absorber and scatterer, λ is the mean free path of the photoelectron, σ² is the mean square radial displacement also known as Debye–Waller factor, δ is the phase shift of the couple absorber/scatterer, and *i* represents a particular number of shell. The goodness of the fit is given by *R*-factor.

Diffuse Reflectance Infra-Red Spectroscopy (DRIFTS): CO adsorption-DRIFTS investigations were carried out on a VERTEX 70 FTIR spectrometer (Bruker) equipped with a Harrick in situ diffuse reflectance cell covered with a CaF₂ window. 100–200 μ catalyst sieve fraction was used for the measurements. Catalysts were purged with Ar via mass flow controller and heated to 353 K to remove the physisorbed species over 1 h. The resulting spectra collected were in reflectance (R) mode at room temperature between 1000–4000 cm⁻¹ with a spectral resolution of 6 cm⁻¹. The spectra were reported according to the Kubelka–Munk (KM) model by converting the reflectance according to the following equation.

$$KM = \frac{(1-R)^2}{2R} \quad (2)$$

For background scans, 200 spectra were collected under He or Ar flow, and for the samples, 150 scans were collected per measurement. The measurements were performed continuously for 1 h. The online gas mixture was constantly monitored by a quadrupole mass spectrometer.

The turnover frequency (TOF) was calculated by the following equation:^[56–58]

$$\text{TOF}(\text{h}^{-1}) = \frac{\text{Moles of evolved H}_2}{\text{Moles of Pt on photocatalysts} \times \text{Reaction time (h)}} \quad (3)$$

Supporting Information

Supporting Information is available from the Wiley Online Library or from the author.

Acknowledgements

The authors would like to acknowledge DFG and the Operational Program Research, Development and Education (European Regional Development Fund, Project No. CZ.02.1.01/0.0/0.0/15_003/0000416 of the Ministry of Education, Youth and Sports of the Czech Republic) for financial support. The authors acknowledge the European Synchrotron Radiation Facility (ESRF, Grenoble, France) for granting the beamtime proposal (CH-6119) and are grateful to Dr. Cesare Atzori and the other beamline staff from BM23 for their assistance in setting up the beamline. The authors thank Jiyun Zhang and Christoph J. Brabec from FAU, Germany, for photoluminescence measurements. The authors also acknowledge Zdenek Badura and Giorgio Zoppellaro from Regional Centre of Advanced Technologies and Materials (RCPTM), Czech Republic, for valuable scientific discussions.

Open access funding enabled and organized by Projekt DEAL.

Conflict of Interest

The authors declare no conflict of interest.

Data Availability Statement

Research data are not shared.

Keywords

diffuse reflectance infra-red spectroscopy, photocatalytic H₂ evolution, photoluminescence, Pt single atoms, TiO₂ polymorphs, X-ray absorption fine structure, X-ray absorption near-edge spectra

Received: April 13, 2022

Revised: May 28, 2022

Published online:

- [1] A. Fujishima, K. Honda, *Nature* **1972**, 238, 37.
- [2] A. L. Linsebigler, G. Lu, J. T. Yates, *Chem. Rev.* **1995**, 95, 735.
- [3] M. Ni, M. K. H. Leung, D. Y. C. Leung, K. Sumathy, *Renewable Sustainable Energy Rev.* **2007**, 11, 401.
- [4] A. Fujishima, X. Zhang, D. A. Tryk, *Surf. Sci. Rep.* **2008**, 63, 515.
- [5] K. Takanebe, *ACS Catal.* **2017**, 7, 8006.
- [6] A. Kudo, *Int. J. Hydrog. Energy* **2006**, 31, 197.
- [7] H. Liu, D. Chen, Z. Wang, H. Jing, R. Zhang, *Appl. Catal. B* **2017**, 203, 300.
- [8] J. Zhang, W. Hu, S. Cao, L. Piao, *Nano Res.* **2020**, 13, 2313.
- [9] Y. Lu, W.-J. Yin, K.-L. Peng, K. Wang, Q. Hu, A. Selloni, F.-R. Chen, L.-M. Liu, M.-L. Sui, *Nat. Commun.* **2018**, 9, 2752.
- [10] L. Qin, G. Wang, Y. Tan, *Sci. Rep.* **2018**, 8, 16198.
- [11] L. Gao, Y. Li, J. Ren, S. Wang, R. Wang, G. Fu, Y. Hu, *Appl. Catal. B* **2017**, 202, 127.
- [12] A. Sclafani, J. M. Herrmann, *J. Phys. Chem.* **1996**, 100, 13655.
- [13] Y. K. Kho, A. Iwase, W. Y. Teoh, L. Mädler, A. Kudo, R. Amal, *J. Phys. Chem. C* **2010**, 114, 2821.
- [14] J. Shi, J. Chen, Z. Feng, T. Chen, Y. Lian, X. Wang, C. Li, *J. Phys. Chem. C* **2007**, 111, 693.
- [15] D. K. Pallotti, L. Passoni, P. Maddalena, F. Di Fonzo, S. Lettieri, *J. Phys. Chem. C* **2017**, 121, 9011.
- [16] F. J. Knorr, C. C. Mercado, J. L. McHale, *J. Phys. Chem. C* **2008**, 112, 12786.
- [17] S. Lv, M. Pei, Y. Liu, Z. Si, X. Wu, R. Ran, D. Weng, F. Kang, *Nano Res.* **2022**.
- [18] J.-J. Zou, H. He, L. Cui, H.-Y. Du, *Int. J. Hydrog. Energy* **2007**, 32, 1762.
- [19] Y. Z. Yang, C. H. Chang, H. Idriss, *Appl. Catal. B* **2006**, 67, 217.
- [20] O. Rosseler, M. V. Shankar, M. K.-L. Du, L. Schmidlin, N. Keller, V. Keller, *J. Catal.* **2010**, 269, 179.
- [21] X. Jiang, X. Fu, L. Zhang, S. Meng, S. Chen, *J. Mater. Chem. A* **2015**, 3, 2271.
- [22] D. Kaplan, M. Alon, L. Burstein, Y. Rosenberg, E. Peled, *J. Power Sources* **2011**, 196, 1078.
- [23] P. Kim, J. B. Joo, W. Kim, J. Kim, I. K. Song, J. Yi, *J. Power Sources* **2006**, 160, 987.
- [24] Z. Jiang, Z. Zhang, W. Shangguan, M. A. Isaacs, L. J. Durndell, C. M. A. Parlett, A. F. Lee, *Catal. Sci. Technol.* **2016**, 6, 81.
- [25] K. Wenderich, G. Mul, *Chem. Rev.* **2016**, 116, 14587.
- [26] J. Xing, J. F. Chen, Y. H. Li, W. T. Yuan, Y. Zhou, L. R. Zheng, H. F. Wang, P. Hu, Y. Wang, H. J. Zhao, Y. Wang, H. G. Yang, *Chem. - Eur. J.* **2014**, 20, 2138.
- [27] B. Wen, W.-J. Yin, A. Selloni, L.-M. Liu, *Phys. Chem. Chem. Phys.* **2020**, 22, 10455.
- [28] C. Jin, Y. Dai, W. Wei, X. Ma, M. Li, B. Huang, *Appl. Surf. Sci.* **2017**, 426, 639.
- [29] T. Li, J. Liu, Y. Song, F. Wang, *ACS Catal.* **2018**, 8, 8450.
- [30] Y. H. Li, J. Xing, X. H. Yang, H. G. Yang, *Chem. - Eur. J.* **2014**, 20, 12377.
- [31] C. Dessal, L. Martínez, C. Maheu, T. Len, F. Morfin, J. L. Rousset, E. Puzenat, P. Afanasiev, M. Aouine, L. Soler, J. Llorca, L. Piccolo, *J. Catal.* **2019**, 375, 155.
- [32] C. Gao, J. Low, R. Long, T. Kong, J. Zhu, Y. Xiong, *Chem. Rev.* **2020**, 120, 12175.
- [33] Z.-H. Xue, D. Luan, H. Zhang, X. W. Lou, *Joule* **2022**, 6, 92.
- [34] S. Hejazi, S. Mohajernia, B. Osuagwu, G. Zoppellaro, P. Andryskova, O. Tomanec, S. Kment, R. Zbořil, P. Schmuki, *Adv. Mater.* **2020**, 32, 1908505.
- [35] S. Qin, N. Denisov, J. Will, J. Kolařík, E. Spiecker, P. Schmuki, *Sol. RRL* **2022**, 6, 2101026.
- [36] G. Cha, I. Hwang, S. Hejazi, A. S. Dobrota, I. A. Pašti, B. Osuagwu, H. Kim, J. Will, T. Yokosawa, Z. Badura, Š. Kment, S. Mohajernia, A. Mazare, N. V. Skorodumova, E. Spiecker, P. Schmuki, *iScience* **2021**, 24, 102938.

- [37] X. Zhou, I. Hwang, O. Tomanec, D. Fehn, A. Mazare, R. Zboril, K. Meyer, P. Schmuki, *Adv. Funct. Mater.* **2021**, *31*, 2102843.
- [38] Z. Wu, I. Hwang, G. Cha, S. Qin, O. Tomanec, Z. Badura, S. Kment, R. Zboril, P. Schmuki, *Small* **2021**, *18*, 2104892.
- [39] Y. Wang, I. Hwang, Z. Wu, P. Schmuki, *Electrochem. Commun.* **2021**, *133*, 107166.
- [40] Y. Chen, S. Ji, W. Sun, Y. Lei, Q. Wang, A. Li, W. Chen, G. Zhou, Z. Zhang, Y. Wang, L. Zheng, Q. Zhang, L. Gu, X. Han, D. Wang, Y. Li, *Angew. Chem., Int. Ed.* **2020**, *59*, 1295.
- [41] Y. Chen, S. Ji, W. Sun, W. Chen, J. Dong, J. Wen, J. Zhang, Z. Li, L. Zheng, C. Chen, Q. Peng, D. Wang, Y. Li, *J. Am. Chem. Soc.* **2018**, *140*, 7407.
- [42] E. Wierzbicka, X. Zhou, N. Denisov, J. Yoo, D. Fehn, N. Liu, K. Meyer, P. Schmuki, *ChemSusChem* **2019**, *12*, 1900.
- [43] S. Qin, H. Kim, N. Denisov, D. Fehn, J. Schmidt, K. Meyer, P. Schmuki, *JPhys Energy* **2021**, *3*, 034003.
- [44] Z. Li, B. Tian, W. Zhen, Y. Wu, G. Lu, *Appl. Catal. B* **2017**, *203*, 408.
- [45] B. Ohtani, *Catalysts* **2013**, *3*, 942.
- [46] W. Choi, J. Y. Choi, H. Song, *APL Mater.* **2019**, *7*, 100702.
- [47] J. R. Harbour, J. Tromp, M. L. Hair, *Can. J. Chem.* **1985**, *63*, 204.
- [48] J. Kiwi, M. Graetzel, *J. Phys. Chem.* **1984**, *88*, 1302.
- [49] N. Liu, S. Mohajernia, N. T. Nguyen, S. Hejazi, F. Plass, A. Kahnt, T. Yokosawa, A. Osvet, E. Spiecker, D. M. Guldi, P. Schmuki, *ChemSusChem* **2020**, *13*, 4937.
- [50] Y. Zhou, D. E. Doronkin, M. Chen, S. Wei, J.-D. Grunwaldt, *ACS Catal.* **2016**, *6*, 7799.
- [51] L. DeRita, S. Dai, K. Lopez-Zepeda, N. Pham, G. W. Graham, X. Pan, P. Christopher, *J. Am. Chem. Soc.* **2017**, *139*, 14150.
- [52] K. Ding, A. Gulec, A. M. Johnson, N. M. Schweitzer, G. D. Stucky, L. D. Marks, P. C. Stair, *Science* **2015**, *350*, 189.
- [53] B. Han, Y. Guo, Y. Huang, W. Xi, J. Xu, J. Luo, H. Qi, Y. Ren, X. Liu, B. Qiao, T. Zhang, *Angew. Chem., Int. Ed.* **2020**, *59*, 11824.
- [54] S. Qin, Z. Badura, N. Denisov, O. Tomanec, S. Mohajernia, N. Liu, S. Kment, G. Zoppellaro, P. Schmuki, *Electrochem. Commun.* **2021**, *122*, 106909.
- [55] B. Ravel, M. Newville, *J Synchrotron Rad.* **2005**, *12*, 537.
- [56] Z. Sun, H. Zheng, J. Li, P. Du, *Energy Environ. Sci.* **2015**, *8*, 2668.
- [57] X. I. Pereira-Hernández, A. DeLaRiva, V. Muravev, D. Kunwar, H. Xiong, B. Sudduth, M. Engelhard, L. Kovarik, E. J. M. Hensen, Y. Wang, A. K. Datye, *Nat. Commun.* **2019**, *10*, 1358.
- [58] S. Kozuch, J. M. L. Martin, *ACS Catal.* **2012**, *2*, 2787.